Clim. Past Discuss., 10, 1381–1420, 2014
www.clim-past-discuss.net/10/1381/2014/
doi:10.5194/cpd-10-1381-2014

Climate of the Past Discussions
Open Access

Evolution of the large-scale atmospheric circulation in response to changing ice sheets over the last glacial cycle

M. Löfverström[1,3], R. Caballero[1,3], J. Nilsson[1,3], and J. Kleman[2,3]

[1]Department of Meteorology, Stockholm University, Stockholm, Sweden
[2]Department of Physical Geography and Quaternary Geology, Stockholm University, Stockholm, Sweden
[3]Bolin Center for Climate Research, Stockholm University, Stockholm, Sweden

Received: 10 March 2014 – Accepted: 19 March 2014 – Published: 4 April 2014

Correspondence to: M. Löfverström (marcus@misu.su.se)

Published by Copernicus Publications on behalf of the European Geosciences Union.

Abstract

We present modelling results of the atmospheric circulation at the cold periods of marine isotope stage 5b (MIS 5b), MIS 4 and the Last Glacial Maximum (LGM), as well as the interglacial. The paleo-simulations are forced by ice sheet reconstructions consistent with geological evidence and by appropriate insolation and greenhouse gas concentrations. The results suggest that the large-scale atmospheric winter circulation remained largely similar to the interglacial for a significant part of the glacial cycle. The proposed explanation is that the ice sheets were located in areas where their interaction with the mean flow is limited. However, the LGM Laurentide Ice Sheet induces a much larger planetary wave that leads to a zonalisation of the Atlantic jet. In summer, the ice sheet topography dynamically induces warm temperatures in Alaska and central Asia that inhibits the expansion of the ice sheets into these regions. The warm temperatures may also serve as an explanation for westward propagation of the Eurasian Ice Sheet from MIS 4 to the LGM.

1 Introduction

Over the last 2.6 million years Earth's climate has fluctuated between cold and warm periods – glacials and interglacials – characterised by the growth of major ice sheets over the Northern Hemisphere continents during cold periods and their retreat during warm periods. The most recent glacial cycle began some 115 000 years ago (115 kyr BP) following a relative minimum in the Northern Hemisphere summer insolation (Berger and Loutre, 2004). Reconstructions of ice-sheet development through the subsequent 90 kyr (Peltier and Fairbanks, 2006; Stokes et al., 2012; Kleman et al., 2013) show global ice volume increasing in a step-wise fashion, with rapid growth bursts followed by longer periods of stagnation and culminating in the Last Glacial Maximum (LGM) spanning 19–23 kyr BP.

CPD
10, 1381–1420, 2014

Initially, distinct ice sheets developed in the Central Canadian Arctic, Quebec, Scandinavia and the Barents–Kara Seas (Kleman et al., 2013), with possible smaller ice masses also in the Canadian Cordillera. An amalgamation process subsequently took place whereby these smaller and spatially separated ice sheets successively coalesced to finally form two massive and coherent ice sheets at the LGM, the Laurentide–Cordilleran ice sheet in North America and the Fenoscandian–Barents Sea ice sheet in Eurasia. At certain times, the mostly independent British–Irish ice sheet also formed part of the Eurasian Ice Sheet. The Laurentide was by far the larger of these LGM ice sheets, filling the northern part of North America from east to west and reaching southwards to approximately 42° N.

The topography of the Northern Hemisphere thus evolved in a rather complex way over the past glacial, starting from the interglacial configuration characterized by two high-elevation areas (Rocky Mountains and the Himalayas), over states with up to four substantial and separated high-elevation areas, to the LGM state with two continental-scale ice sheets. Large-scale topography affects climate by exciting stationary Rossby waves, manifested as planetary-scale meanders in the time-mean atmospheric zonal flow (see the review by Held et al., 2002). In the interglacial regime, the Rossby wave train forced by flow over the Rocky Mountains (in conjunction with thermal forcing over the Gulf Stream region, Kaspi and Schneider, 2011) induces north-westerly flow over central and eastern North America, yielding harsh winters there. The topographically-driven wave is also largely responsible for the north-eastward tilt of the Atlantic jet (Brayshaw et al., 2009), contributing to the milder winters of Europe compared with similar latitudes in North America (Seager et al., 2002).

Much effort has been devoted to understanding the circulation and climate of the LGM, including comprehensive proxy data syntheses (e.g. MARGO, 2009), combined data-model reconstructions (Dail and Wunsch, 2014) and a large range of modelling studies, notably within the Paleoclimate Modelling Intercomparison Projects[1] (PMIP 1 & 2) (Braconnot et al., 2007). Though there are appreciable model-to-model and

[1] http://pmip.lsce.ipsl.fr/, http://pmip2.lsce.ipsl.fr/

CPD
10, 1381–1420, 2014

model-data discrepancies (Li and Battisti, 2008; Otto-Bliesner et al., 2009), these studies generally depict an LGM climate substantially different from present. This is especially true in the Atlantic sector, which exhibits pronounced cooling of the northern North Atlantic Ocean, southward displacement of the sea-ice margin and southward-shifted, more zonally-oriented atmospheric jet stream and storm tracks. Model-based decomposition of the various factors involved shows that these changes can be primarily attributed to the mechanical forcing of the circulation induced by the Laurentide Ice Sheet's massive topography, rather than to increased albedo or reduced CO_2 (Pausata et al., 2011).

The circulation during the long build-up phase to the LGM has received much less attention, despite the importance of this time-wise dominant period for understanding how the ocean, atmosphere and cryosphere reorganized as the world transitioned from an interglacial to a full-glacial state. Today, it is well established that important terrestrial glaciation traces can only be understood in the context of glacial configurations predating the LGM and of less than full-glacial size (Ljungner, 1949; Kleman, 1992; Fredin, 2002; Kleman et al., 2008). The significance of this long but less than full-glacial time period was recognized by Porter (1989), who coined the term "average glacial" conditions.

An important unanswered question about the pre-LGM climate is whether this "average glacial" climate had more in common with LGM or with interglacial conditions. Though smaller than they would eventually become at the LGM, the North American ice sheets nonetheless presented a Rocky Mountains-sized topographic obstacle over eastern North America even in the early stages of the last glacial (Kleman et al., 2013). It is thus conceivable that they could have affected the circulation significantly, bringing it closer to the full LGM regime.

Another key issue is the extent to which atmospheric perturbations induced by pre-LGM ice sheets helped shape the evolution of the ice sheets themselves. Studies using idealized coupled atmosphere–ice-sheet models focusing on the dynamics of a single continental-scale ice sheet on a flat continent (Roe and Lindzen, 2001; Liakka

CPD
10, 1381–1420, 2014

et al., 2011; Liakka, 2012) show that stationary wave–ice sheet interaction can strongly influence both the spatial form and the temporal evolution of the ice sheet. Remote interactions between widely separated ice sheets mediated by stationary Rossby waves have received less attention, though there have been suggestions that the North American ice sheets excited a stationary wave train acting to warm north-western Europe, suppressing ice growth there and potentially explaning why the Eurasian Ice Sheet was considerably smaller than the Laurentide in the latter stages of the glaciation (Roe and Lindzen, 2001). Similar questions arise regarding the documented absence of major ice sheets in places where they could be expected, such as Alaska and East-central Siberia, and the reasons for the general south-westward migration of the Eurasian Ice Sheet through the last glacial cycle.

Here, we explore these questions using a general circulation model (GCM) to simulate the atmospheric circulation's response to changing topography – taken from the geologically-constrained ice-sheet reconstruction of Kleman et al. (2013) – at four representative time-slices spanning the last glacial. The modelling strategy is described in detail in Sect. 2. The main results of the study are presented in Sect. 3 and discussed in Sect. 4. Section 5 summarises our conclusions.

2 Model and experiments

2.1 Model

We employ the National Center for Atmospheric Research Community Atmospheric Model version 3 (CAM3) (Collins et al., 2004, 2006), using a spectral dynamical core with T85 (approximately 1.4°) horizontal resolution and 26 hybrid sigma-pressure levels in the vertical. Continental surfaces – including prescribed ice sheets – are represented by the Community Land Model version 3 (CLM3) (Oleson et al., 2004). The ocean is represented by a motionless slab of fixed heat capacity, with ocean heat transport (OHT) represented by a prescribed climatological seasonally-varying energy

CPD
10, 1381–1420, 2014




convergence field. The slab ocean also contains a thermodynamic sea-ice model. Further details on the prescription of the ice sheets and OHT are given below.

2.2 Ice sheets

Continental ice sheets over North America and Eurasia are prescribed from the recent reconstruction described by Kleman et al. (2013), to which the reader is referred for full details. Briefly, the reconstruction spans the last glacial and employs a numerical ice sheet model (specifically, the University of Maine Ice Sheet Model (UMISM), Fastook and Chapman, 1989; Fastook, 1993) constrained by geological and geomorphological data. While reasonably reliable data constraints for ice sheet margins during pre-LGM times are available in some locations, other regions are less well constrained, and there are no constraints at all on ice sheet elevations and cross-sectional profiles. The strategy employed by Kleman et al. (2013) was to tune the ice sheet model's mass balance forcing using global model parameters to match well-constrained outline segments as closely as possible where such constraints exist while relying on the model physics to capture ice sheet elevations and outlines in unconstrained regions. This procedure bears some analogies to data assimilation, where a physically-based model is used as an optimal extrapolator or predictor for regions or fields not directly constrained by data.

The resulting evolution of global ice volume is shown in Fig. 1, and is a good qualitative match to previous reconstructions of global ice volume and inferences from sea-level data (Peltier and Fairbanks, 2006; Stokes et al., 2012). Snapshots of the spatial distribution of the ice sheets are shown in Fig. 2 and discussed further below.

UMISM outputs the net surface elevation, combining the topographic height with the ice thickness and isostatic depression of the bedrock due to ice loading, on a rectangular grid with 100×100 points, covering approximately 45° N to the North Pole. This dataset is interpolated to T85 resolution and combined with the present day topography to create a paleo-topography with global coverage for use in the present

CPD
10, 1381–1420, 2014

simulations. We assume full glaciation of grid cells where the paleo-data is at least 250 m higher than the present day topography.

2.3 Ocean Heat Transport (OHT)

Since a considerable number of runs are required to elucidate the evolution of the circulation over the past glacial, use of a fully-coupled ocean–atmosphere model is unfeasible for the present study. Resorting to the more computationally efficient slab ocean model comes at the price of uncertainty regarding the impact of changes in ocean circulation. If the atmospheric circulation is very sensitive to OHT, results obtained with an arbitrarily prescribed OHT may be of little relevance to the real world. To address this problem we use two end-member OHT prescriptions, corresponding to interglacial conditions and to the LGM respectively, which presumably bracket the range of OHTs over the last glacial. The two OHT specifications are derived from corresponding equilibrated simulations of the fully-coupled version of the NCAR model (the Community Climate System Model version 3) under respectively pre-industrial and LGM conditions (Brandefelt and Otto-Bliesner, 2009). All the simulations to be described below were carried out twice, once with interglacial and once with LGM OHT (with modern-day annual-mean mixed layer depths used to specify the slab's heat capacity in all cases). Comparison between these twin simulations permits an assessment of the sensitivity to OHT in each case. As it turns out, there are some modest quantitative differences between the two sets of simulations, but the overall qualitative conclusions of the study are robust to changes in OHT.

2.4 Experiments

As shown in Fig. 1, global ice volume during the last glacial grew in three main surges centered around ~ 110, ~ 70, and ~ 25 kyr, while remaining roughly constant for extended periods in between. To capture the main features of this evolution, we focus on 4 time-slices representative of the main stages of the glacial cycle:

CPD
10, 1381–1420, 2014

– interglacial (Fig. 2a). This case represents conditions prior to inception of the last glacial and during modern, pre-industrial conditions. It employs modern topography and pre-industrial greenhouse gas concentrations and orbital parameters.

– Marine Isotope Stage 5b (MIS 5b, ~ 88 200 kyr BP, Fig. 2b). Already at this relatively early stage of the glacial cycle, the ice sheets are of a significant size. In Eurasia they cover the Arctic coast from Scandinavia to central Siberia and stand about 2000 m high. In North America there are two ice sheets, both in the east of the continent – the Keewatin Dome in the eastern Canadian archipelago and the Quebec Dome on the Labrador Peninsula – that are beginning to merge and form a single entity as high and wide as the Rockies. At this stage, the Eurasian and North American ice sheets contain about the same ice volume.

– MIS 4 (~ 66 000 kyr BP, Fig. 2c). Around half-way into the glacial cycle, the ice volume in North America is now roughly twice as large as in Eurasia and consists of the two-domed proto-Laurentide Ice Sheet and a number of smaller freestanding ice sheets in the Cordilleran region. The Keewatin Dome covers most of the Canadian archipelago and north-central parts of the Candian mainland. In the north, a small gap to the Rocky Mountains still exists, widening to approximately 1000 km futher south. On the northeastern and southeastern fringes, towards Baffin Bay and the North Atlantic, ice everywhere reaches the sea. The Quebec Dome is the larger of the two (the figure suggest the opposite but that is due to the map projection) and extend almost as far south as 42° N over the eastern continent. The Eurasian Ice Sheet is here at its maximum zonal extent. Both the Eurasian and proto-Laurentide Ice Sheet are in this case about 2500 m high.

– LGM (MIS 2, ~ 20 000 kyr BP, Fig. 2d). Under full glacial conditions, the Laurentide Ice Sheet is a single-domed continent-wide entity that dwarfs the Rockies. The center of mass is in the middle of the continent, as in the ICE-5G reconstruction

CPD
10, 1381–1420, 2014

(Peltier, 2004) used in PMIP2. Our reconstruction of the Laurentide ice dome is lower, however, about 3500 m as compared to about 4500 m in ICE-5G. In Eurasia the ice margin has retreated in the east and shifted the center of mass to Scandinavia, but achieves its greatest meridional extent and even covers most of the British Isles.

For each glacial simulation, we set the orbital clock to the nominal time of the ice sheet reconstruction. We also adjust the concentrations of long-lived greenhouse gases to typical values estimated from the EPICA Dome C ice-core (Petit et al., 1999; Spahni et al., 2005), see Table 1. These values are rounded off to the nearest 5 ppmv for the CO_2 and 5 ppbv for the CH_4 and N_2O. The concentrations of chlorofluorocarbons (CFC_{11} and CFC_{12}) are identically zero in all simulations and we use the pre-industrial aerosol distribution. All simulations use modern pre-industrial vegetation cover adjusted by the glacier mask.

To test the sensitivity of the results to orbital parameters and greenhouse gas concentrations, we conduct an additional set of simulations in which topography is held fixed at its interglacial distribution while orbital parameters and greenhouse gases take on glacial values. For the MIS 4 case we also run two additional simulations where the Eurasian and North American ice sheets are removed in turn to further investigate their relative influence on the atmospheric flow patterns. A list of the various combinations of boundary conditions used in this study is shown in Table 2. Results presented below are based on seasonal averages over 30 years after the simulated climates have reached statistical equilibrium. The spin-up of the model takes about 20–30 model years and the climate is assumed to have equilibrated when the long-term trends in the global and annual mean surface temperature and sea-ice concentration become negligible.

CPD
10, 1381–1420, 2014

3 Results

This section presents the main results from the simulations of the 4 time slices discussed above. For brevity we present only results from the interglacial and MIS 5b simulations with interglacial OHT and MIS 4 and LGM simulation with LGM OHT; as noted in Sect. 2.3, changing OHT does not affect our qualitative conclusions.

3.1 Surface temperature

As shown in Table 3, global-mean surface temperatures continuously decrease across the simulations, dropping by about 5 °C from the interglacial to the LGM irrespective of season. In sensitivity simulations in which the ice sheets are eliminated (indicated by asterisks in the table), the temperature drop is only about 3.4 °C; this implies that the ice sheets themselves account for about 1/3 of the global temperature decrease from interglacial to LGM. This differs from the situation in Antarctica, where sensitivity studies with the same model used here show no appreciable temperature change when the Antarctic ice sheet is eliminated (Goldner et al., 2013).

The mean Northern Hemisphere equator–pole temperature gradient generally increases as temperatures cool, in line with expectations of polar-amplified cooling (Singarayer and Valdes, 2010), though interestingly the LGM has a slightly smaller gradient than MIS 4. The gradient grows by around 25 % from the interglacial to the LGM in winter and almost 40 % in summer; this leads to substantial strengthening of the midlatitude westerlies with important consequences for the response to topography, as discussed below.

3.2 Evolution of the winter circulation

Figure 3 shows the climatological 300 hPa eddy geopotential height field (an eddy is defined here as a deviation from the zonal mean) in boreal winter (December–February, DJF) for the 4 time slices. The corresponding zonal winds are shown in Fig. 4. The

CPD
10, 1381–1420, 2014

interglacial eddy heights in the North American/Atlantic sector (Fig. 3a) show a pattern familiar from present-day observations, with a wave train arcing from western North America to North Africa; this pattern is generally interpreted as a stationary Rossby wave excited by the midlatitude westerlies flowing over the Rockies and then refracting into the subtropics where it is absorbed (Held et al., 2002). The Atlantic midlatitude jet in this simulation (Fig. 4a) is somewhat stronger than in present-day observations but its axis has the characteristic southwest–northeast tilt (Brayshaw et al., 2009, 2011) that is also imparted to the Atlantic storm track, as evidenced by the precipitation field.

The results from the glacial simulations suggest that the interglacial disposition of the stationary waves and zonal jet was maintained for a significant portion of the glacial cycle, despite the massive changes in the boundary conditions. At MIS 5b one can only see minor circulation changes and even though the amplitudes of the stationary height anomalies are generally greater at MIS 4, the geopotential height gradients maintain a similar basic disposition. The Atlantic jet is also stronger in this case, but the axial tilt remains largely unchanged. The LGM, however, presents a distinctly different circulation, especially in the Atlantic region. The trough downstream of the fully developed Laurentide Ice Sheet is deep and zonally extensive, yielding a strong and essentially zonal jet. A similar result was obtained by Li and Battisti (2008) using the fully coupled CCSM3 (Community Climate System Model version 3) with LGM boundary conditions following the PMIP2 protocol.

The sea-ice margin (Fig. 2) moves equatorward in both ocean basins as the glacial progresses. However, the North Atlantic remains largely ice-free through MIS 5b, and even in MIS 4 the ice margin has a clear north-eastward tilt parallel to the prevailing winds, presumably because warm advection by the winds prevents sea-ice formation off Western Europe. It is only at the LGM, when the winds become perfectly zonal, that the ice line reaches south to Iberia. Note that the sea-ice cover obtained in our LGM simulation is more extensive than in many other studies, especially in the northeastern Atlantic Ocean. The reason is that the OHT prescription used here is based on the second LGM equilibrium state discussed by Brandefelt and Otto-Bliesner (2009), which

CPD
10, 1381–1420, 2014

is believed to be close to the models true statistical equilibrium. In this state the Atlantic Meridional Overturning Circulation (AMOC) is strongly reduced and sea-ice is therefore able to form over a larger area of the ocean, see their Fig. 2.

Consistenly with the discussion above, there are only limited changes in the precipitation field at MIS 5b and MIS 4 (Fig. 4), and a considerably larger change at the LGM where the storm track is zonalised. The LGM storm track is also more meridionally confined and the precipitation does not reach as far inland over Eurasia as in the previous cases, likely because the more extensive sea-ice cover in the North Atlantic limits evaporation and yields drier air masses moving into Europe. Neither case shows a significant amount of winter precipitation on the ice sheets themselves. There is some precipitation falling on the south-western and western edges but almost nothing in the interior. In Eurasia this is due to the ice sheets' northerly location, where the bulk of the precipitation falls south of the main ice sheet. The North American continent is shielded from the Pacific cyclones by the Rockies, making the air in the interior of the continent relatively dry and less prone to precipitate. We will see later that the picture is different in the summer season.

We can make use of the low-level winds in Fig. 2 to give a rationale for the evolution of the planetary waves. The topography of the Rockies yields an upstream ridge over the eastern Pacific as part of the Rossby wave response, adding anticyclonic curvature of the mean flow: as the air flows onto the topography the effective column depth decreases and the mean flow deflects southwards to conserve potential vorticity. On the eastern side of the mountain range the situation is the opposite and the mean flow follows a cyclonic path as a response to the increasing fluid depth (see the Appendix A for a discussion on potential vorticity conservation). A consequence of the meridional deflection of the mean flow is that the strongest low-level winds are channelled between the Rockies and the incipient Laurentide ice sheet, with little flow normal to the ice sheet topography. Consequently, the mechanical stationary wave forcing by the ice sheet is small, and the outline of the planetary waves remains largely similar to the present day.

CPD
10, 1381–1420, 2014

This explanation is applicable to MIS 5b and partly also MIS 4, as the low-land corridor in the interior of the North American continent is present in both cases. However, in the latter case the westward expansion of the Keewatin Dome in northern Canada partially pinches off the channel, forcing flow over the ice sheet in the north. Further south, the flow crosses the Rockies in a similar fashion as in the interglacial, but overall there is a more substantial interaction between the ice sheets and the mean flow which is reflected in an amplified planetary wave response and an eastward shift of the lee-side trough from the Hudson Bay to the Labrador Sea.

The topographic profile of the LGM Laurentide Ice Sheet is structurally very different from the earlier stages of the glacial cycle. The ice volume is nearly twice as large as at MIS 4 (Fig. 1), and the low-land region east of the Rockies is entirely filled up and instead constitutes the highest part of the continent. Consequently, the topographic blocking is much more substantial than earlier, and the low-level wind field over the eastern Pacific (Fig. 2d) is subject to an even stronger meridional splitting. In fact, the entire flow normal to the ice sheet is blocked and forced on a poleward track. A similar meridional splitting was also found by Manabe and Broccoli (1985) and Cook and Held (1988). Note that the blocking high over the north-eastern Pacific is strong enough to even force low-level easterlies over parts of Alaska and Siberia. This is also hinted in Fig. 3d where the upper tropospheric anticyclone is significantly stronger than earlier and protrude far into eastern Siberia.

The Eurasian Ice Sheet topography is located too far to the north to be able to interact with the strong midlatitude zonal-mean flow and thereby influence the stationary wave field. In both MIS 5b and MIS 4 the strongest westerly winds are found over Central Europe, whereas the southern ice margin is located over Scandinavia. Even though the ice sheet expands equatorward when moving into the LGM, the zonalisation of the Atlantic storm track shifts the westerly winds southwards and the flow-topography interaction therefore remains small.

CPD
10, 1381–1420, 2014

3.3 Evolution of the summer circulation (JJA)

The reduced equator-to-pole temperature gradient in the summer season yields a more quiescent troposphere and zonal asymmetries in the circulation are driven to a larger extent by radiative heating contrasts than by mechanical forcing. The outline and vertical structure of the summer stationary waves is therefore quite different from those in winter. The pressure anomalies over the continents resemble the summer monsoon, with thermally induced cyclones near the surface and high pressure anomalies aloft caused by divergent flow at higher levels. The opposite polarity of the eddy geopotential is found over the oceans; see White (1982) and Ting (1994) for comprehensive discussions on the summer stationary waves.

Figure 5 shows the upper tropospheric eddy geopotential averaged over the summer months. One can readily see a progressive development of the wave field over the course of the glacial cycle. Already at MIS 5b there is some amplification of the height anomalies over the northern parts of North America and one can also see an additional wave train propagating over the Atlantic Ocean into Europe. The response does resemble the linear topographic wave, or low mountain wave, discussed by, e.g., Valdes and Hoskins (1991), Cook and Held (1992), Ringler and Cook (1997). The amplitude of these waves is clearly linked to the size of the ice topography as they are reinforced but stay in approximately the same location when the ice sheets grow larger. The anticyclone over North America is therefore split up into one part forced thermally, and one part induced mechanically by the ice sheet topography at higher latitudes. As the ice sheets evolve, the anticyclone at higher latitudes becomes dominant and the thermal high is gradually being marginalised and shifted southwards. A systematic development of the wave field can also be seen in Eurasia. The upper tropospheric anticyclone in eastern Siberia is both strengthened and shifted westwards in time and becomes a substantial feature in the region. Due to the relatively weak mean flow (see Fig. 6) there is little downstream wave propagation, but the high pressure ridge is strongly amplified by the diabatic cooling over the ice sheet (Ringler and Cook, 1999; Liakka, 2012).

CPD
10, 1381–1420, 2014

Figure 6 shows the spatial distribution of the summer precipitation. The tropics dominates the picture but one can clearly see that the midlatitude storm tracks are weaker and less organized than in winter and the precipitation is therefore dispersed over a larger area. The warm air transports water vapor far inland and precipitates over the ice sheets. One can also see a precipitation maximum on the windward side of the ice sheets that encourage their westward expansion in time. There is also an additional maximum along the southern edge of the Eurasian Ice Sheet that is a result of the anticyclonic circulation in Fig. 5. Likewise, the drier conditions east of the Eurasian Ice Sheet at the LGM comes from advection of cold air in the southward branch of the circulation cell.

To maintain the ice sheets over the warm season the total mass loss from melting and ablation has to be balanced by the accumulation of snow over the year. The question is therefore how the changes in the atmospheric circulation influence the surface temperature field. To investigate we use the parallel sequence of simulations with identical forcing as in the three glacial simulations but with the interglacial topography; by subtracting the surface temperature in the no-ice sheet cases from the glacial simulations, we obtain a qualitative idea of how the climate responds to the presence of the large-scale ice sheets and therefore how the ice sheets affect their own maintenance. Note that two forcing agents – topography and surface albedo – change between the no-ice sheet and glacial simulations. We make no attempt to decompose this further.

Results from the sensitivity experiments are shown in Fig. 7. It is apparent that the presence of the ice sheets has a large influence on both the regional temperature and cloud cover. The Atlantic sector features a progressively expanding area of cooling while there are relative warm anomalies in Alaska and Central Asia. A similar warm anomaly southeast of the Eurasian Ice Sheet has been found in previous studies of the LGM, see e.g. Manabe and Broccoli (1985), Rind (1987), Felzer et al. (1996, 1998), Abe-Ouchi et al. (2007). Warmer temperatures in Alaska were also reported by e.g.

CPD
10, 1381–1420, 2014

Otto-Bliesner et al. (2006) and Abe-Ouchi et al. (2007), where the latter compared the LGM and interglacial temperatures from several different models.

The increasingly dominant anticyclonic circulation over Alaska and Siberia implies subsiding motion there and therefore generally reduced cloudiness as seen in Fig. 7. The land surface thus absorbs a larger amount of downwelling shortwave radiation, which leads to warmer temperatures. The anticyclonic circulation also implies warm air advection into the target areas that helps to increase the temperatures even further.

The strongly diminished temperature anomaly in Eurasia in the LGM simulation (Fig. 7e) is somewhat at odds with this picture, however, since the anticyclone is at its strongest. This weakening of the warm anomaly is likely the result of cold westerly temperature advection from the Atlantic (which remains ice-covered through the summer, Fig. 2d) and counteracts the radiative heating in Siberia. This does not happen to the same extent in MIS 4 as the anticyclone is located farther to the east and the temperatures in Europe are not as low as at the LGM.

The colder surface temperature in the Atlantic region is a result of the extensive sea-ice cover. Figure 2 shows that in winter, the North American ice sheets force strong northerly winds that advect cold polar air over the eastern parts of the continent and also the western Atlantic. The cold air advection thus helps to shift the sea-ice line farther equatorward than it would if the ice sheet was not present. In the warm season the extensive sea-ice limits the evaporation over the northern North Atlantic and results in a net reduction of the cloudiness as seen in the right column in Fig. 7. A reduced cloudiness implies more down-welling of shortwave radiation but the melting process of snow and sea-ice is slow and inefficient due to the high surface albedo. The colder air over the ocean is also advected by the westerly winds to Europe where it holds down the surface temperature and helps sustain and build the western part of the Eurasian Ice Sheet over the warm season. Note that the LGM simulation features an area of increased cloudiness south of the sea-ice margin that is not reflected in the precipitation pattern. A decomposition (not shown) reveals that this is related to a larger fraction of

CPD
10, 1381–1420, 2014

low-level clouds. We make no attempt to evaluate the processes involved in generating this signal.

To further establish the connection between the temperature anomalies and the different ice sheets we have conducted an additional set of simulations for the MIS 4 case where only one of the Laurentide and Eurasian Ice Sheets are present. The corresponding temperature difference is shown in Fig. 8. It is obvious that most of the temperature response in the western hemisphere and Europe is linked to the presence of the Laurentide Ice Sheet, whereas the relative temperature anomaly in Asia is a result of the circulation change induced by the Eurasian Ice Sheet.

4 Discussion

4.1 Winter stationary waves

The results presented in Figs. 3 and 4 show some very substantial changes in the winter stationary waves, Atlantic jet stream and storm tracks between the interglacial and LGM. These changes do not come about as a smooth progression through time, however. Our MIS 5b simulation, which is representative of the first 30–40 kyr of the glacial (see Fig. 1), shows a circulation essentially unchanged from the interglacial, despite the considerable ice sheets developing in eastern North America and Eurasia. Stationary wave amplitudes increase during the subsequent 30–40 kyr, represented by our MIS 4 simulation, and the jet strengthens considerably, but the overall structure of the stationary waves remains very similar to that in the interglacial – retaining, in particular, the characteristic southwesterly tilt of the Atlantic jet. It is arguably only in the LGM simulation, representing some 5–10 kyr around the peak of the last glacial, that qualitative changes can be seen, with a full zonalization of the jet and a perceptible shift towards more zonally elongated stationary wave structures: note that throughout the interglacial, MIS 5b and MIS 4 simulations there are 3 peaks and troughs in the eddy height field along latitude lines in the midlatitudes (Fig. 3a–c), while there are clearly only 2 in the LGM simulation.

CPD
10, 1381–1420, 2014

The shift toward longer stationary waves is consistent with the predictions of simple linear barotropic theory (see Appendix A). A key result of the theory is that the stationary wavenumber $K_s = \sqrt{\beta/[u]}$, where $[u]$ is the zonal-mean zonal wind and β is the meridional gradient of the Coriolis parameter. As discussed in Sect. 3.1, the equator-to-pole temperature gradient increases as the LGM is approached resulting in stronger winds (the zonal-mean wind averaged betwen 800 and 150 hPa increases by about 30 % from 18 $m s^{-1}$ in the interglacial to 24 $m s^{-1}$ in the LGM simulation) and thus smaller K_s, or longer stationary waves. In addition, the zonal width of the North American orography – which forces the stationary wave train over the Atlantic – increases very substantially from the interglacial to the LGM, so that the forcing of the stationary waves also shifts towards longer scales.

The muted response to ice sheets in the early stages of the glaciation is a nonlinear effect. The North American ice sheets begin their development in the trough downwind of the Rockies, with the ice margin roughly parallel to the mean flow, where they cannot efficiently excite stationary waves (as this requires flow normal to the topography). This is a nonlinear – or, more precisely, finite-amplitude – effect since it is the superposition of the wave generated by the Rockies onto the zonal-mean basic flow that yields the muted response; in the linear approximation, waves are excited only by the basic flow. Note that it is not by chance that the ice sheets develop where they do: it is precisely the northwesterly advection by the pre-existing flow that creates favourably cold conditions over northeastern North America. We therefore expect this to be a robust effect, replicated also in other models (so long as they faithfully reproduce the interglacial flow).

A similar effect occurs for the Eurasian Ice Sheet, which also fails to excite stationary waves in the early stages of the glacial. In this case, warm southwesterly advection by the Atlantic jet presumably limits the southward extension of the Fennoscadian ice sheet, automatically confining this ice sheet to a region of weak climatological westerlies which are unable to excite large stationary waves.

CPD
10, 1381–1420, 2014

Although the simple linear model captures the main features of the LGM stationary waves with suprising quantitative accuracy, this is likely a fortuitous result the choice of parameter values and in particular of the model's channel geometry (Held, 1983). It therefore cannot be concluded that the LGM and interglacial responses presented here are truly linear. GCM simulations by Cook and Held (1992) show that substantial deviations from linearity are possible as topographic height increases, and these deviations are complex and model-dependent (Held et al., 2002). In fact, model intercomparison exercises show a wide range of responses by different models all driven by the same LGM topography (Li and Battisti, 2008); among these, the model used here (CAM3) has a larger-than-average response, with most other models showing an LGM circulation that departs less dramatically from the interglacial (but note that Li and Battisti, 2008, found good agreement between their LGM results using CAM3 and available proxy data). Overall, the robust conclusion that may be drawn from this discussion is that the atmospheric circulation's response to ice sheets during winter was muted through large parts of the last glacial cycle, and possibly even at the LGM.

4.2 Self-induced temperature anomalies in summer

A key factor controlling the evolution of the ice sheets is the summer surface temperature, as it is in the warm season that significant ablation occurs. The temperature at the top of the ice sheets is generally below freezing and the summer ablation is therefore restricted to the marginal ablation zones at lower elevation. Figure 7 shows that the presence of the ice sheets induces warm surface temperature anomalies in Alaska and Siberia. A similar temperature response has been obtained in previous modelling studies of the sensitivity to the LGM ice sheets, e.g. Manabe and Broccoli (1985), Rind (1987), Felzer et al. (1996, 1998), Abe-Ouchi et al. (2007), Otto-Bliesner et al. (2006). That the model simulates warmer temperatures in these particular regions is intriguing, as we know from geological evidence that Alaska was left largely ice-free over the entire glacial cycle (Clague, 1989). At the same time, the

CPD
10, 1381–1420, 2014

Eurasian ice complex was limited to the northernmost parts of the continent and its center of mass shifted southwestwards as the glacial proceeded. In the simulations the summer surface temperature in Alaska stays approximately the same as in the interglacial climate throughout the entire glacial cycle and the region south of the Eurasian Ice Sheet at MIS 4 is even slightly warmer than in the interglacial simulation (not shown). It is thus conceivable that the self-induced warm anomaly in central Siberia may have contributed to limit the glaciation in this region. This warm anomaly may also be a reason for the westward shift of the ice sheet when moving from MIS 4 to the LGM.

5 Conclusions

We summarize our conclusions as follows:

- during winter, the pre-existing stationary wave response to the Rocky Mountains limits the flow's interaction with the ice sheets during MIS 5b and 4, and the influence of these ice sheets on the tropospheric circulation is therefore surprisingly small despite their very substantial size.
- During MIS 5b and 4, the general outline of the winter stationary waves is largely unchanged from the interglacial and the jet axis in the Atlantic sector retains the characteristic southwest–northeast tilt.
- Only when the Laurentide Ice Sheet is fully developed are the planetary waves strongly influenced and the Atlantic jet axis is zonalised as a result. A highly simplified linear stationary wave model suggests that the increased mean wind speed during the LGM is the key parameter controlling the structural changes in the circulation.
- In the summer season, on the contrary, the ice sheets strongly influence the eddy geopotential field and an anticyclonic circulation develops in Alaska and Central Asia as a result. Anticyclonic circulation implies less cloudiness and more

CPD
10, 1381–1420, 2014

shortwave radiation can therefore reach the surface. It is thus plausible that Alaska and Central Asia were left largely ice-free due to self-induced warm anomalies at the surface.

– The North American MIS 5b and 4 ice sheets have a fairly weak remote influence on the conditions over Eurasian Ice Sheet in the present simulations. The most pronounced "downstream response" is cooling over northwestern Europe and warming in northern Siberia during summer. Thus, this remote influence does not straightforwardly explain the relative smallness of Eurasian Ice Sheet, but may have contributed slightly to the westward shift of the ice-sheet mass centre.

– We propose that even though the LGM is the most spectacular phase of the last glacial cycle, it only makes up for a small fraction of its total duration and is not the best representative for the average glacial climate. Most of the last glacial cycle was spent in what can be decribed as a slightly perturbed interglacial circulation regime.

Appendix A

A1 Notes on linear stationary wave theory

We here present some background on linear stationary wave theory that is helpful for the interpretation of the simulated atmospheric flows. The potential vorticity is a conserved[2] property for all fluid elements that essentially measures the ratio between the absolute vorticity and the effective fluid depth. Rossby (1940) showed that for a non-viscous barotropic fluid this can be expressed as

[2]Note that true conservation of potential vorticity is only possible for idealized frictionless and strictly adiabatic fluids.

CPD
10, 1381–1420, 2014

$$\frac{\mathrm{D}}{\mathrm{D}t}\left(\frac{f+\zeta}{H}\right)=0, \tag{A1}$$

where $\mathrm{D}/\mathrm{D}t = \left(\partial/\partial t + \boldsymbol{v}\cdot\boldsymbol{\nabla}\right)$ is the material derivative, $\boldsymbol{v} = (u, v)$ is a vector containing the zonal and meridional components of the wind field and $\boldsymbol{\nabla} = (\partial/\partial x, \partial/\partial y)$ is the horizontal gradient operator. The numerator is here the sum of the planetary (f) and relative vorticity ($\zeta \equiv \hat{\boldsymbol{k}}\cdot\boldsymbol{\nabla}\times\mathbf{v}$) and H is the fluid depth. Equation (A1) says that if the fluid depth change, e.g. by a topographic obstacle, the absolute vorticity has to change in the same direction to conserve their internal ratio.

Assuming a low amplitude topographic forcing ($h_\mathrm{T} \ll H$) and linearizing around a time-independent quasi-geostrophic zonal mean flow ($u = [u] + u^*$, $v = v^*$ where $v^* \sim u^* \ll [u]$, here $[\cdot]$ and $(^*)$ denotes zonal mean and zonal perturbation quantities respectively) at a midlatitude β-plane ($f = f_0 + \beta y$), we can define the perturbation velocity field from a geostrophic streamfunction as $(u^*, v^*) = \hat{\boldsymbol{k}}\times\boldsymbol{\nabla}\psi^*$ and thus $\zeta^* = \nabla^2\psi^*$. The resulting equation has wave solutions of the form $(\psi^*, h_\mathrm{T}) = Re(\psi_0, h_0)\exp i(kx + ly)$ and the complex amplitude of the height anomaly is

$$\psi_0 = \frac{f_0}{H}\frac{h_0}{K^2 - K_\mathrm{S}^2 - iR}, \tag{A2}$$

where $K = \sqrt{k^2 + l^2}$ is the total wave number and the stationary wave number is defined as

$$K_\mathrm{S} = \sqrt{\frac{\beta}{[u]}}. \tag{A3}$$

We have also added a linear damping ($R = rK^2/k[u]$) to ensure bounded solutions as Eq. (A2) resonates for a total wave number equal to the stationary wave number. A stronger wind implies a smaller wave number and thus longer stationary waves. The

CPD
10, 1381–1420, 2014

amplitude of the waves, however, is proportional to the magnitude of the topography. This highly simplified linear model thus suggests that the structural changes in the stationary wave field at the LGM is a result of the increased mean wind speed as it projects onto a smaller stationary wave number. The massive changes in the surface topography merely give more weight to the resonant wave.

To quantify this premise we compute the standard deviation of the wave solution in Eq. (A2) ($\sigma = \sqrt{[\psi_0^2]}$) as a function of the zonal mean wind speed when using the interglacial and LGM topographic profiles at midlatitudes (Fig. 9c and d). We apply the original model settings used by Charney and Eliassen (1949), $f_0 = f(45^\circ\mathrm{N})$, H = 8 km and a meridional wave number with the half-wavelength equals 35° in latitude but a weaker damping, r^{-1} = 20 days, to make the resonant peaks more distinct. These results are presented in Fig. 9e, clearly showing how the model resonates for lower stationary wave numbers as the wind speed increases. It is apparent that the larger topography at the LGM primarily influence the amplitude of the stationary waves. For wind speeds around 20 m s^{-1}, the LGM topography yields amplitudes almost a factor of two larger than the interglacial topography. Figure 6.1 in Held (1983) shows an example of how a similar curve change for various strength of the damping time scale.

Figure 9a and b shows a comparison of the 500 hPa eddy geopotential height from the atmospheric circulation model in the interglacial and LGM simulations with the mid-tropospheric eddy field computed by the linear model. We here use the average tropospheric zonal mean wind speeds in winter (pressure weighted between 800 and 150 hPa) and a damping time scale of r^{-1} = 5 days as in Charney and Eliassen (1949). The zonal mean wind speed in the interglacial and LGM simulation is about 18 and 24 m s^{-1} respectively. Both the GCM and the simple linear model yield a dominant wavenumber 3 anomaly in the interglacial case and a wavenumber 2 pattern in the LGM. The amplitudes of the waves are also comparable, suggesting that the Charney–Eliassen model has some predictive skills. However, as discussed by Held (1983), one has to be cautious when interpreting the results from the linear model. The solution is restricted to a one dimensional barotropic channel flow with no meridional propagation

CPD
10, 1381–1420, 2014

of waves and it only accounts for the topographic forcing. Stationary waves in the real atmosphere tend to follow great circles rather than latitude circles (Hoskins and Karoly, 1981) and additional forcing mechanism and dissipative effects are important for the stationary wave field (e.g. Held et al., 2002).

Acknowledgements. We thank David Battisti for useful discussion and Jenny Brandefelt for providing the LGM climatology used in the computation of the LGM ocean heat transport. This work was financially supported by the Swedish Research Council and the simulations were performed on resources provided by the Swedish National Infrastructure for Computing (SNIC) at National Supercomputing Centre (NSC), Linköping.

References

Abe-Ouchi, A., Segawa, T., and Saito, F.: Climatic Conditions for modelling the Northern Hemisphere ice sheets throughout the ice age cycle, Clim. Past, 3, 423–438, doi:10.5194/cp-3-423-2007, 2007. 1395, 1396, 1399

Berger, A. and Loutre, M.-F.: Astronomical theory of climate change, J. Phys. IV, 121, 1–35, 2004. 1382

Braconnot, P., Otto-Bliesner, B., Harrison, S., Joussaume, S., Peterchmitt, J.-Y., Abe-Ouchi, A., Crucifix, M., Driesschaert, E., Fichefet, Th., Hewitt, C. D., Kageyama, M., Kitoh, A., Laîné, A., Loutre, M.-F., Marti, O., Merkel, U., Ramstein, G., Valdes, P., Weber, S. L., Yu, Y., and Zhao, Y.: Results of PMIP2 coupled simulations of the Mid-Holocene and Last Glacial Maximum – Part 1: experiments and large-scale features, Clim. Past, 3, 261–277, doi:10.5194/cp-3-261-2007, 2007. 1383

Brandefelt, J. and Otto-Bliesner, B. L.: Equilibration and variability in a Last Glacial Maximum climate simulation with CCSM3, Geophys. Res. Lett., 36, L19712, doi:10.1029/2009GL040364, 2009. 1387, 1391

Brayshaw, D. J., Hoskins, B., and Blackburn, M.: The basic ingredients of the North Atlantic storm track, Part I: Land–sea contrast and orography, J. Atmos. Sci., 66, 2539–2558, 2009. 1383, 1391

Brayshaw, D. J., Hoskins, B., and Blackburn, M.: The basic ingredients of the North Atlantic storm track, Part II: Sea surface temperatures., J. Atmos. Sci., 68, 1784–1805, 2011. 1391

CPD
10, 1381–1420, 2014

Charney, J. G. and Eliassen, A.: A numerical method for predicting the perturbations of the middle latitude westerlies, Tellus, 1, 38–54, doi:10.1111/j.2153-3490.1949.tb01258.x, 1949. 1403

Clague, J. J.: Quaternary Geology of the Canadian Cordillera, Geological Society of America, Boulder, CO, 1989. 1399

Collins, W. D., Rasch, P. J., Boville, B. A., Hack, J. J., McCaa, J. R., Williamson, D. L., Kiehl, J. T., Briegleb, B., Bitz, C., Lin, S.-J., Zhang, M., and Dai, Y.: Description of the NCAR Community Atmosphere Model (CAM3), Tech. Rep. NCAR/TN464-STR, National Center for Atmospheric Research, Boulder, CO, 226 pp., 2004. 1385

Collins, W. D., Rasch, P. J., Boville, B. A., Hack, J. J., McCaa, J. R., Williamson, D. L., Briegleb, B., Bitz, C., Lin, S.-J., and Zhang, M.: The Formulation and Atmospheric Simulation of the Community Atmosphere Model Version 3 (CAM3), J. Climate, 19, 2144–2161, 2006. 1385

Cook, K. H. and Held, I. M.: Stationary waves of the ice age climate, J. Climate, 1, 807–819, 1988. 1393

Cook, K. H. and Held, I. M.: The stationary response to large-scale orography in a general circulation model and a linear model, J. Atmos. Sci., 49, 525–539, 1992. 1394, 1399

Dail, H. and Wunsch, K.: Dynamical Reconstruction of Upper-Ocean Conditions in the Last Glacial Maximum Atlantic, J. Climate, 27, 807—823, 2014. 1383

Fastook, J. L.: The finite-element method for solving conservation equations in glaciology, Comput. Sci. Eng., 1, 55–67, 1993. 1386

Fastook, J. L. and Chapman, J.: A map plane finite-element model: three modeling experiments, J. Galciol., 35, 48–52, 1989. 1386

Felzer, B., Oglesby, R. J., Webb, T., and Hyman, D. E.: Sensitivity of a general circulation model to changes in Northern Hemisphere ice sheets, J. Geophys. Res., 101, 19077–19092, 1996. 1395, 1399

Felzer, B., Webb III, T., and Oglesby, R. J.: The impact of ice sheets, CO_2, and orbital insolation on late quaternary climates: sensitivity experiments with a general circulation model, Quaternary Sci. Rev., 17, 507–534, 1998. 1395, 1399

Fredin, O.: Conference: International workshop on inceptions – mechanisms, patterns and timing of ice sheet inception, Idre Mountain station, Sweden, 17–21 June 2001, Quatern. Int., 95, 99–112, 2002,. 1384

Goldner, A., Huber, M., and Caballero, R.: Does Antarctic glaciation cool the world?, Clim. Past, 9, 173–189, doi:10.5194/cp-9-173-2013, 2013. 1390

CPD
10, 1381–1420, 2014

Held, I. M.: Stationary and quasi-stationary eddies in the extratropical troposphere: theory, in: Large-Scale Dynamical Processes in the Atmosphere, edited by: Hoskins, B. J. and Pearce, R. P., Academic Press, New York, 127–168, 1983. 1399, 1403
Held, I. M., Ting, M., and Wang, H.: Northern winter stationary waves: theory and modeling, J. Climate, 16, 2125–2144, 2002. 1383, 1391, 1399, 1404
Hoskins, B. J. and Karoly, D. J.: The steady linear response of a spherical atmosphere to thermal and orographic forcing, J. Atmos. Sci., 38, 1179–1196, 1981. 1404
Kaspi, Y. and Schneider, T.: Winter cold of eastern continental boundaries induced by warm ocean waters, Nature, 471, 621–624, 2011. 1383
Kleman, J.: The palimpsest glacial landscape in northwestern Sweden – Late Weichselian deglaciation landforms and traces of older west-centered ice sheets, Geogr. Ann., 74A, 305–325, 1992. 1384
Kleman, J., Lundqvist, J., and Stroeven, A. P.: Patterns of Quaternary ice sheet erosion and deposition in Fennoscandia, Geomorphology, 97, 73–90, 2008. 1384
Kleman, J., Fastook, J., Ebert, K., Nilsson, J., and Caballero, R.: Pre-LGM Northern Hemisphere ice sheet topography, Clim. Past, 9, 2365–2378, doi:10.5194/cp-9-2365-2013, 2013. 1382, 1383, 1384, 1385, 1386
Li, C. and Battisti, D.: Reduced Atlantic Storminess during Last Glacial Maximum: evidence from a coupled climate model, J. Climate, 21, 3561–3579, 2008. 1384, 1391, 1399
Liakka, J.: Interactions between topographically and thermally forced stationary waves: implications for ice-sheet evolution, Tellus A, 64, 11088, doi:10.3402/tellusa.v64i0.11088, 2012. 1385, 1394
Liakka, J., Nilsson, J., and Löfverström, M.: Interactions between stationary waves and ice sheets: linear versus nonlinear atmospheric response, Clim. Dynam., 38, 1249–1262, 2011. 1384
Ljungner, E.: East-west balance of the Quaternary ice caps in Patagonia and Scandinavia, Bulletin of the Geol. Inst. of Uppsala, 11–96, 1949. 1384
Manabe, S. and Broccoli, A.: The influence of continental ice sheets on the climate of an ice age, J. Geophys. Res., 90, 2167–2190, 1985. 1393, 1395, 1399
MARGO: Constraints on the magnitude and patterns of ocean cooling at the Last Glacial Maximum, Nat. Geosci., 2, 127–132, 2009. 1383
Oleson, K. W., Dai, Y., Bonan, G., Bosilovich, M., Dickinson, R., Dirmeyer, P., Hoffman, F., Houser, P., Levis, S., Niu, G.-Y., Thornton, P., Vertenstein, M., Yang, Z.-L., and Zeng, X.:

CPD
10, 1381–1420, 2014




Technical description of the Community Land Model (CLM), Tech. Rep. NCAR/TN-461STR, National Center for Atmospheric Research, Boulder, CO, 174 pp., 2004. 1385
Otto-Bliesner, B. L., Brady, E. C., Clauzet, G., Tomas, R., Levis, S., and Kothavala, Z.: Last glacial maximum and Holocene climate in CCSM3, J. Climate, 19, 2526–2544, 2006. 1396, 1399
Otto-Bliesner, B. L., Schneider, R., Brady, E. C., Kucera, M., Abe-Ouchi, A., Bard, E., Braconnot, P., Crucifix, M., Hewitt, C. D., Kageyama, M., Marti, O., Paul, A., Rosell-Mele, A., Waelbroeck, C., Weber, S. L., Weinelt, M., and Yu, Y.: A comparison of PMIP2 model simulations and the MARGO proxy reconstruction for tropical sea surface temperatures at last glacial maximum, Clim. Dynam., 32, 799–815, 2009. 1384
Pausata, F. S. R., Li, C., Wettstein, J. J., Kageyama, M., and Nisancioglu, K. H.: The key role of topography in altering North Atlantic atmospheric circulation during the last glacial period, Clim. Past, 7, 1089–1101, doi:10.5194/cp-7-1089-2011, 2011. 1384
Peltier, W.: Global glacial isostasy and the surface of the ice-age Earth: the ICE-5G (VM2) model and GRACE, Annu. Rev. Earth Pl. Sc., 32, 111–149, 2004. 1389
Peltier, W. and Fairbanks, R. G.: Global glacial ice volume and Last Glacial Maximum duration from an extended Barbados sea level record, Quaternary Sci. Rev., 25, 3322–3337, 2006. 1382, 1386
Petit, J.-R., Jouzel, J., Raynaud, D., Barkov, N. I., Barnola, J.-M., Basile, I., Bender, M., Chappellaz, J., Davis, M., Delaygue, G., Delmotte, M., Kotlyakov, V. M., Legrand, M., Lipenkov, V. Y., Lorius, C., Pepin, L., Ritz, C., Saltzman, E., and Stievenard, M.: Climate and atmospheric history of the past 420,000 years from the Vostok ice core, Antarctica, Nature, 399, 429–436, 1999. 1389
Porter, S. C.: Some geological implications of average Quaternary glacial conditions, Quaternary Res., 32, 245–261, 1989. 1384
Rind, D.: Components of the ice age circulation, J. Geophys. Res., 92, 4241–4281, 1987. 1395, 1399
Ringler, T. D. and Cook, K. H.: Factors controlling nonlinearity in mechanically forced stationary waves over orography, J. Atmos. Sci., 54, 2612–2629, 1997. 1394
Ringler, T. D. and Cook, K. H.: Understanding the seasonality of orographically forced stationary waves: Interaction between mechanical and thermal forcing, J. Atmos. Sci., 56, 1154–1174, 1999. 1394

CPD
10, 1381–1420, 2014

Roe, G. H. and Lindzen, R. S.: The Mutual Interaction between Continental-Scale Ice Sheets and Atmospheric Stationary Waves, J. Climate, 14, 1450–1465, 2001. 1384, 1385
Rossby, C.-G.: Planetary flow patterns in the atmosphere, Q. J. Roy. Meteor. Soc., 66, 68–87, 1940. 1401
Seager, R., Battisti, D. S., Yin, J., Gordon, N., Naik, N., Clement, A. C., and Cane, M. A.: Is the Gulf Stream responsible for Europe's mild winters?, Q. J. Roy. Meteor. Soc., 128, 2563–2586, 2002. 1383
Singarayer, J. S. and Valdes, P. J.: High-latitude climate sensitivity to ice-sheet forcing over the last 120 kyr, Quaternary Sci. Rev., 29, 43–55, 2010. 1390
Spahni, R., Chappellaz, J., Stocker, T. F., Loulergue, L., Hausammann, G., Kawamura, K., Flückiger, J., Schwander, J., Raynaud, D., Masson-Delmotte, V., and Jouzel, J.: Atmospheric methane and nitrous oxide of the late Pleistocene from Antarctic ice cores, Science, 310, 1317–1321, 2005. 1389
Stokes, C. R., Tarasov, L., and Dyke, A. S.: Dynamics of the North American Ice Sheet Complex during its inception and build-up to the Last Glacial Maximum, Quaternary Sci. Rev., 50, 86–104, 2012. 1382, 1386
Ting, M.: Maintenance of northern summer stationary waves in a GCM, J. Atmos. Sci., 51, 3286–3308, 1994. 1394
Valdes, P. J. and Hoskins, B. J.: Nonlinear orographically forced planetary waves, J. Atmos. Sci., 48, 2089–2106, 1991. 1394
White, G. H.: An observational study of the Northern Hemisphere extratropical summertime general circulation, J. Atmos. Sci., 39, 24–40, 1982. 1394

CPD
10, 1381–1420, 2014

Table 1. Concentrations of long-lived greenhouse gases in the different simulations. All instances are given per volume.

	CO_2	CH_4	N_2O
IG	280 ppm	760 ppb	270 ppb
MIS 5b	210 ppm	450 ppb	240 ppb
MIS 4	195 ppm	460 ppb	215 ppb
LGM	185 ppm	350 ppb	200 ppb

CPD
10, 1381–1420, 2014

Table 2. Configuration of boundary conditions used in the study (marked by ×). The oceanic heat fluxes for interglacial and LGM conditions are denoted by Q_{IG} and Q_{LGM} and the interglacial and reconstructed paleo-topography by Φ_{IG} and Φ_{Paleo} respectively. The sensitivity tests of the paleo-topography with only the North American or Eurasian Ice Sheets present are denoted by Φ_{NA} and Φ_{EA}.

	Q_{IG}				Q_{LGM}			
	Φ_{IG}	Φ_{Paleo}	Φ_{NA}	Φ_{EA}	Φ_{PI}	Φ_{Paleo}	Φ_{NA}	Φ_{EA}
IG	×	–	–	–	×	–	–	–
MIS 5b	×	×	–	–	×	×	–	–
MIS 4	×	×	×	×	×	×	×	×
LGM	×	×	–	–	×	×	–	–

CPD
10, 1381–1420, 2014

Table 3. Global-mean surface temperature T_m (°C) and Northern Hemisphere equator–pole (average from 0–10 to 80–90° N) temperature difference ΔT (°C) for the 4 time slices. Asterisks indicate sensitivity simulations employing interglacial topography.

		IG	MIS 5b	MIS 4	LGM	MIS 5b*	MIS 4*	LGM*
Annual	T_m	12.7	10.0	9.1	7.6	10.9	9.5	9.3
	ΔT	47.0	50.9	63.1	60.2	47.0	58.1	58.2
DJF	T_m	10.8	7.3	6.2	5.2	8.1	6.8	6.9
	ΔT	64.6	71.2	82.7	80.0	66.2	77.1	77.8
JJA	T_m	14.6	12.7	12.0	10.1	13.7	12.2	11.6
	ΔT	25.8	25.5	36.8	34.9	24.5	33.0	32.9

CPD
10, 1381–1420, 2014

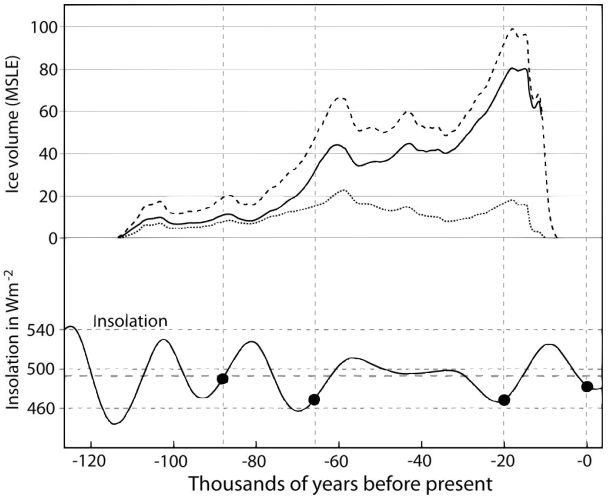

Fig. 1. Evolution of the Northern Hemisphere ice volume and variations in daily average top of the atmosphere insolation in northern summer solstice (60° N) as a function of time. The solid and dotted lines in the top panel show the volume of the North American and Eurasian Ice Sheets respectively and the dashed line is the total ice volume. The black dots in the lower panel mark the relative time of the simulations and thick dashed line shows the mean insolation over the time period.

CPD
10, 1381–1420, 2014

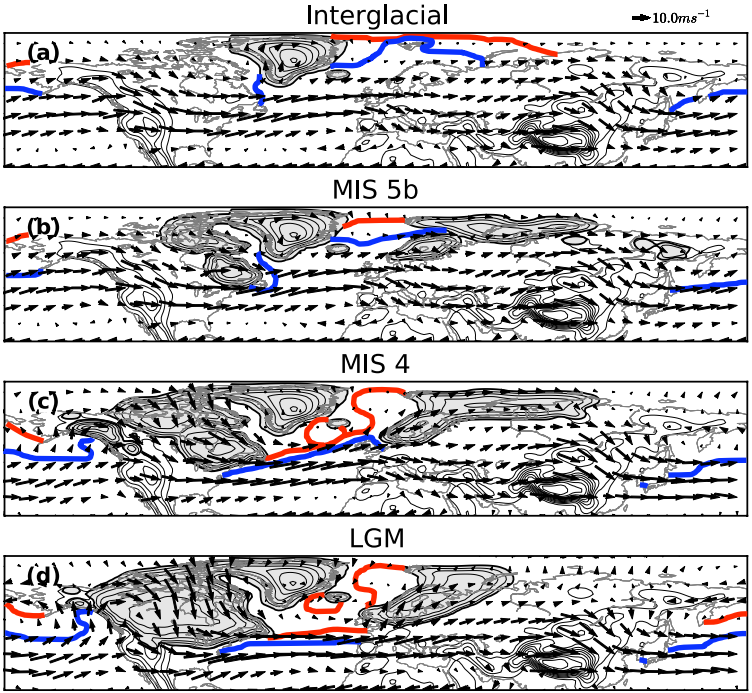

Fig. 2. Evolution of the Northern Hemisphere topography over the glacial cycle (shading of ice sheets). The contour interval is 500 m and the outer contour line defines the edge of the ice sheets. The arrows show the wind vectors in winter along a model level (the nominal 800 hPa surface) and the blue (red) line the 50 % sea-ice margin in winter (summer).

CPD
10, 1381–1420, 2014

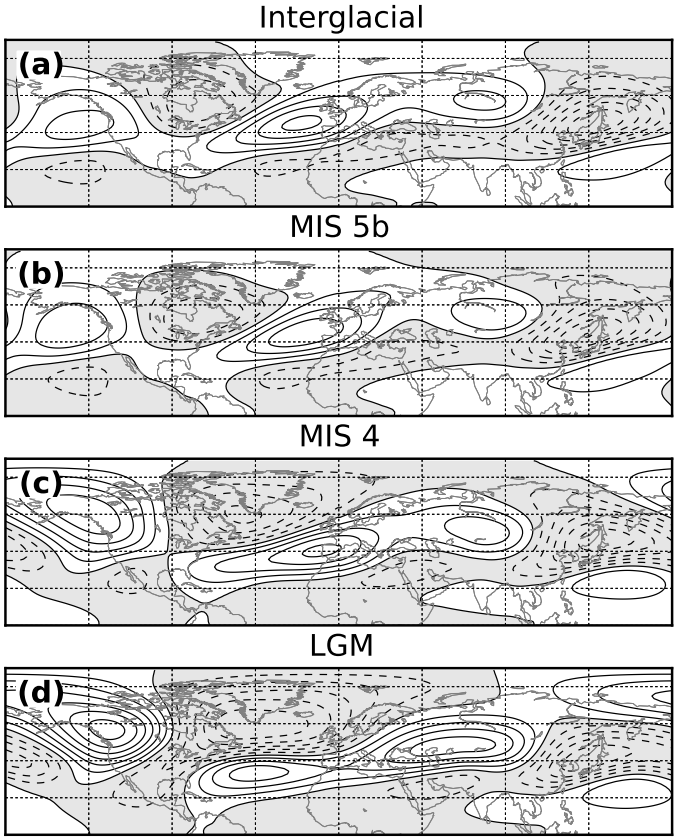

Fig. 3. The 300 hPa eddy geopotential field averaged over the winter months (DJF). Contour lines every 50 m and negative values are shaded. Note the zonalisation of the geopotential height gradient over the Atlantic Ocean in the LGM simulation.

CPD
10, 1381–1420, 2014

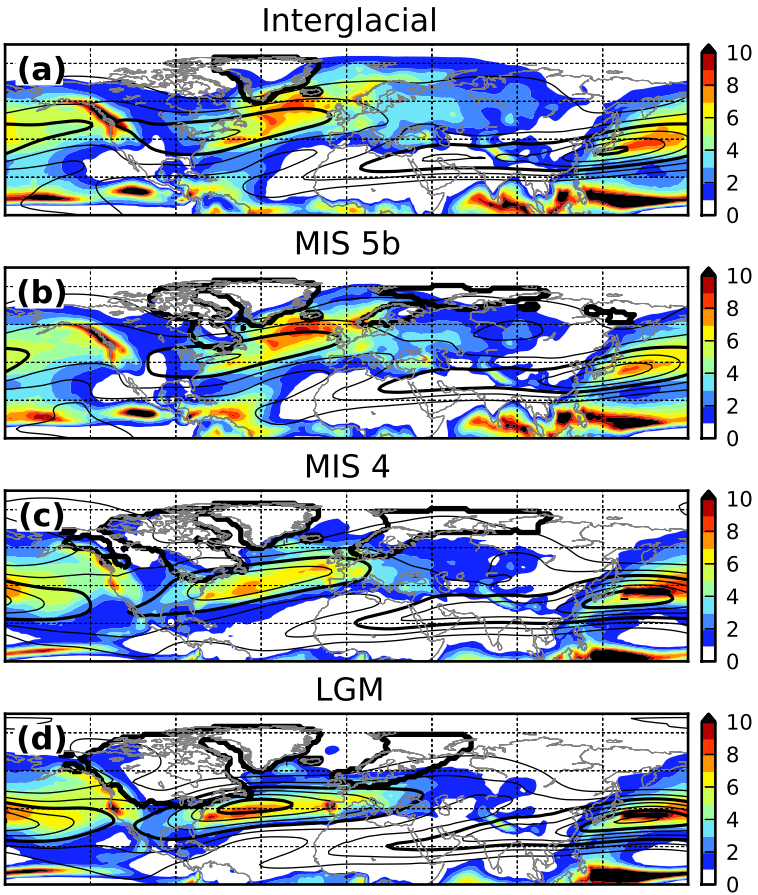

Fig. 4. Evolution of the winter (DJF) precipitation (mm day^{-1}) over the glacial cycle. The ice sheets are indicated by the heavy contours and the thinner lines show the 300 hPa zonal wind speed with a contour interval of 10 m s^{-1}. The 30 and 60 m s^{-1} contours are thicker.

CPD
10, 1381–1420, 2014

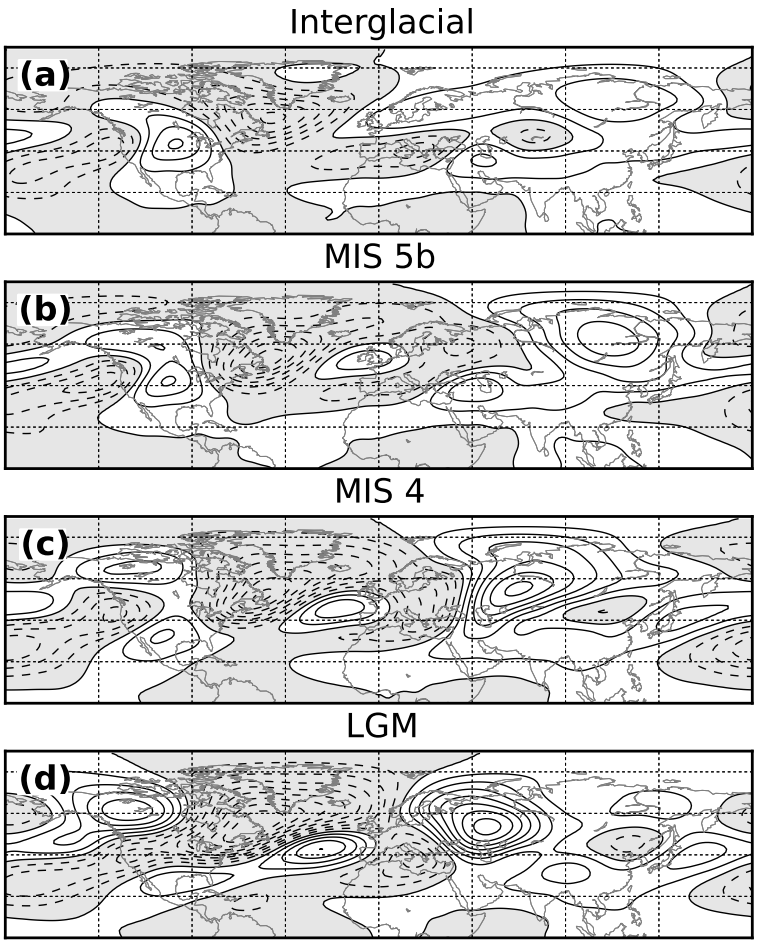

Fig. 5. Evolution of the 300 hPa eddy geopotential in the summer (JJA) season. Contour lines every 25 m and negative values are shaded.

CPD
10, 1381–1420, 2014

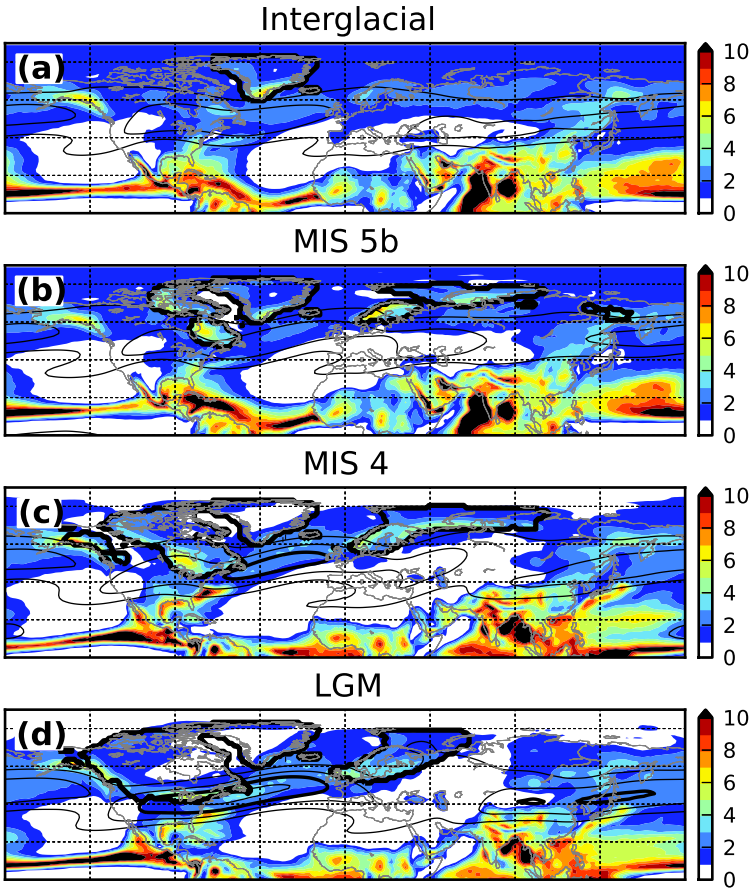

Fig. 6. Evolution of the summer (JJA) precipitation (mm day^{-1}) over the glacial cycle. The ice sheets are indicated by the heavy contours and the thinner lines show the 300 hPa zonal wind speed with a contour interval of 10 m s^{-1}. The 30 m s^{-1} contour is thicker.

CPD
10, 1381–1420, 2014

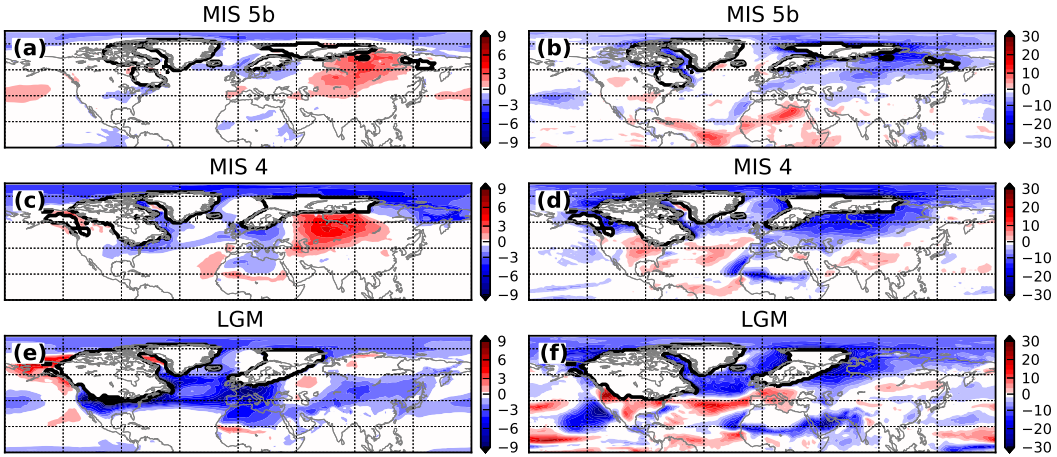

Fig. 7. The left column shows the difference in average summer (JJA) surface temperature (K) between the full glacial simulations and the no-ice sheet simulations, see details in the text. The right column shows the corresponding difference in the total cloudiness (%). Note that values over the ice sheets are masked out for display purposes.

CPD
10, 1381–1420, 2014

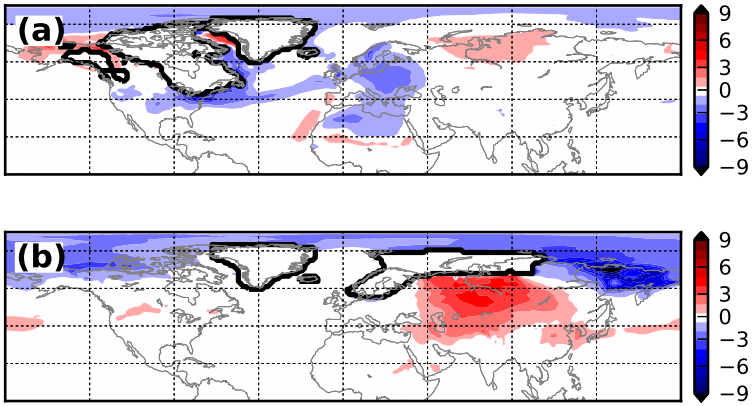

Fig. 8. Same as in Fig. 7c but split up for the MIS 4 Laurentide Ice Sheet topography in the upper panel and the Eurasian Ice Sheet topography in the lower panel.

CPD
10, 1381–1420, 2014

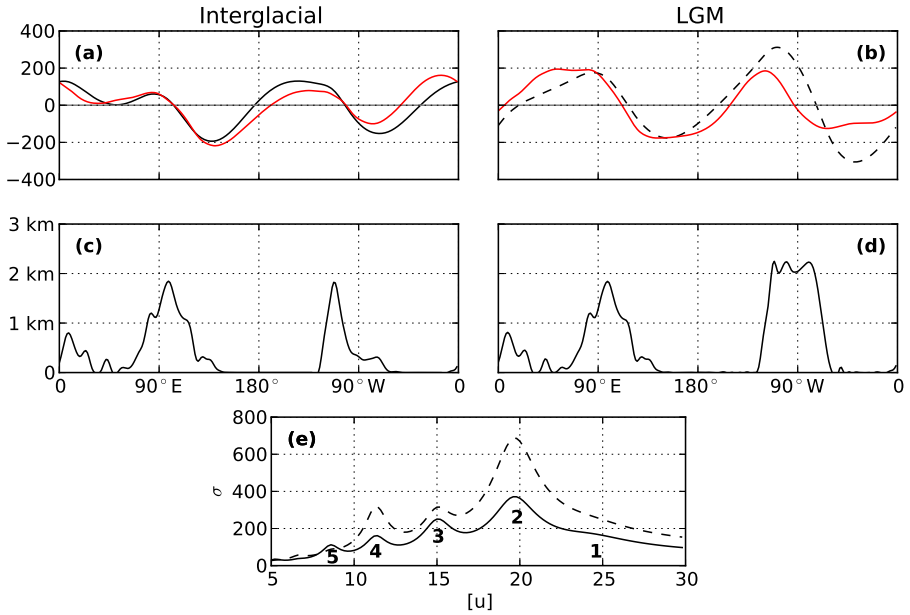

Fig. 9. The top panels **(a, b)** show a comparison of the mid-tropopsheric eddy geopotential (m) at 45° N computed by the linear barotropic model (black) and the atmospheric circulation model (red) at 500 hPa. The left column shows the interglacial and the right panel the fields from the LGM simulations. The corresponding topographic profiles are shown in the middle panels **(c, d)**. In the lower panel **(e)** we show the standard deviation of the geopotential height response ($\sigma = \sqrt{[\psi_0^2]}$) as a function of the zonal mean wind $[u]$. Here we use a more generous damping time scale of $r^{-1} = 20$ days for display purposes. One can clearly see how different wave numbers resonates at certain wind speeds. The solid line use the present day topography **(c)** and the dashed line the LGM topography **(d)**.

CPD
10, 1381–1420, 2014